Design and Performance of 40 cm Ion Optics[*][†]

George C. Soulas
NASA Glenn Research Center
M.S. 301-3
21000 Brookpark Road
Cleveland, OH 44135, U.S.A.
216-977-7419
George.C.Soulas@grc.nasa.gov

IEPC-01-090

A 40 cm ion thruster is being developed at the NASA Glenn Research Center to obtain input power and propellant throughput capabilities of 10 kW and 550 kg, respectively. The technical approach here is a continuation of the "derating" technique used for the NSTAR ion thruster. The 40 cm ion thruster presently utilizes the NSTAR ion optics aperture geometry to take advantage of the large database of lifetime and performance data already available. Dome-shaped grids were chosen for the design of the 40 cm ion optics because this design is naturally suited for large-area ion optics. Ion extraction capabilities and electron backstreaming limits for the 40 cm ion optics were estimated by utilizing NSTAR 30 cm ion optics data. A preliminary service life assessment showed that the propellant throughput goal of 550 kg of xenon may be possible with molybdenum 40 cm ion optics. One 40 cm ion optics' set has been successfully fabricated to date. Additional ion optics' sets are presently being fabricated. Preliminary performance tests were conducted on a laboratory model 40 cm ion thruster.

Nomenclature

A_{dome}	Domed grid area, m²
d	Grid aperture diameter, m
d_b	Beam extraction diameter, m
e	Electron charge, C
E_{eff}	Effective elastic modulus of the perforate grid region, Pa
f_{corr}	Sputter yield correction factor
F_{dome}	Fractional change of the grid area from doming
f_{flat}	Beam flatness parameter (ratio of average-to-peak beam current density)
F_g	Accelerator grid view factor
F_{oa}	Grid open area fraction
F_t	Beam divergence thrust correction factor
g	Acceleration of gravity, m/s²
h	Height of the grid dome, m
J_b	Beam current, A
j_b	Beam current density, A/m²
J_i	Accelerator grid impingement current, A
k_B	Boltzmann's constant, J/K
k_{corr}	Correction factor for peak beam current density, V·m²/A
l_e	Effective acceleration length, m
l_g	Grid cold gap, m
l_n	Neutralization length, m
l_{up}	Upstream potential well location, m
m_{amu}	Atomic mass of grid material, amu
$\dot{m}_d$	Discharge chamber mass flow rate, kg/s
m_i	Ion mass, kg
m_n	Propellant atomic mass, kg
N	Neutral density distribution function
n	Number of gravities (i.e. g-load)
N_A	Avogadro's number, mol⁻¹
n_b	Facility background neutral density, m⁻³
n_d	Discharge chamber neutral density, m⁻³
n_n	Neutral density distribution upstream of the neutralization plane, m⁻³
NPH	Normalized perveance per hole, A/V^{3/2}

---

[*]Presented as Paper IEPC-01-090 at the 27th International Electric Propulsion Conference, Pasadena, CA, 15-19 October, 2001.
[†]This paper is declared a work of the U.S. Government and is not subject to copyright protection in the United States.

NPH_{corr}	Correlated normalized perveance per hole, $A/V^{3/2}$
r_c	Chord radius of domed grid, m
R_{dome}	Radius of curvature for the grid dome, m
R_j	Ratio of doubly-to-singly charged ion current
R^0_{max}	Maximum net-to-total accelerating voltage extrapolated to a zero beam current
T	Thrust, N
T_g	Grid temperature, K
T_n	Neutral propellant temperature, K
T_s	Stiffener temperature, K
t_s	Screen grid thickness, m
V_b	Beam voltage, V
V_d	Discharge voltage, V
V_{eb}	Electron backstreaming limit voltage, V
V_t^{lim}	Impingement-limited total voltage, V
$\dot{V}'_{p-g}$	Accelerator grid pit and groove volumetric erosion rate per aperture, m^3/s
$\dot{V}'_s$	Screen grid volumetric erosion rate per aperture, m^3/s
$\dot{V}'_w$	Accelerator grid aperture wall volumetric erosion rate per aperture, m^3/s
Y	Sputter yield at an orthogonal angle of incidence
z	Axial dimension, m
α	Thrust correction factor for doubly-to-singly charged ion current
α_g	Grid material thermal expansion coefficient, $1/C°$
α_s	Stiffener material thermal expansion coefficient, $1/C°$
η_d^{++}	Discharge chamber propellant utilization efficiency accounting for doubly charged ions
θ_{max}	Maximum dome angle from the grid axial centerline, rad
ν_{eff}	Effective Poisson's ratio of the perforate grid region
π	Pi (3.141593)
ρ	Grid material mass density, kg/m^3
ρ_{eff}	Effective mass density of the perforate grid region, kg/m^3
σ_{c-e}	Charge-exchange cross-section, m^2
σ_{hoop}^{max}	Peak circumferential (i.e. hoop) stress, Pa
σ_{merid}^{max}	Peak meridional stress, Pa
φ	Neutral transparency of the ion optics
φ_i	Screen grid transparency to discharge ions

Superscripts

a	Accelerator grid
avg	Average
dwn	Charge-exchange ions created downstream of the neutralization plane
hot	Temperature during thruster operation
n	Orthogonal to the grid surface
NSTAR	NSTAR ion thruster
pk	Peak
rt	Room temperature
s	Screen grid
up	Charge-exchange ions created upstream of the neutralization plane
´	Per aperture
+	Singly charged ion
++	Doubly charged ion

Subscripts

a	Accelerator grid
s	Screen grid

Introduction

The success of the NSTAR (i.e. NASA Solar Electric Propulsion Technology Applications Readiness Program) 30 cm ion thruster system on the Deep Space 1 mission has demonstrated the viability of ion propulsion for deep space missions.[1,2] As a result, ion propulsion is a candidate for several deep space missions, such as the Neptune Orbiter, Titan Explorer, Mars Sample Return, Europa Lander, and others. However, ion propulsion system mass and volume could be significantly reduced for many of these missions by increasing the NSTAR thruster's propellant throughput and peak input power capabilities beyond the 140 kg and 2.3 kW, respectively, demonstrated by past and ongoing wear tests.[3-5] Propulsion system mass and volume reductions occur because fewer thrusters and, therefore, fewer accompanying power processors and propellant feed system components, would be required.

Increasing propellant throughput and thruster power is limited, in part, by sputter erosion of the ion optics.[6,7] Significant charge-exchange accelerator grid sputter erosion can lead to electron backstreaming due to accelerator aperture enlargement, grid structural failure due to pit and groove erosion of the downstream surface, or an unclearable grid short by a

flake from sputter-eroded accelerator grid material. Significant screen grid sputter erosion by discharge chamber ions can lead to structural failure of the screen grid, as well as exacerbating the aforementioned accelerator grid failure mechanisms from direct beam ion impingement.

Long duration tests in the NSTAR program[3-5] and others[6,7] have demonstrated, however, that sputter erosion of the downstream surface and aperture walls of the accelerator grid must be addressed to increase ion optics' longevity. Wear test results from Ref. [3] have shown that screen grid sputter erosion is minimal for the NSTAR thruster, likely due to the derated operating conditions of this engine. Although screen grid erosion must be addressed in any ion optics' service life assessment, lifetimes well beyond those demonstrated in Refs. [3]-[5] are expected as long as the low discharge voltages and plasma densities are maintained and the ratio of doubly-to-singly charged ions is not significantly increased.

Several methods of extending ion optics' service life are presently being pursued at the NASA Glenn Research Center (GRC).[8] One method involves changing the ion optics' material to one with a lower volumetric sputter erosion rate than molybdenum. Grid material technologies presently investigated include carbon-based materials, titanium, and ion-implanted materials.[8-11] Another method for increasing ion optics service life involves increasing the accelerator grid thickness to provide more material for sputter erosion.[12] This prevents the loss of the large database already available with molybdenum ion optics while providing an anticipated 2x improvement in accelerator grid service life. While all of these methods allow for increases in thruster propellant throughput and input power, most improvements are anticipated to be modest if the 30 cm thruster diameter is maintained.[9]

To obtain input power and propellant throughput capabilities of 10 kW and 550 kg, respectively, a 40 cm ion thruster is being developed at the NASA GRC.[13] This engine has twice the beam area as the NSTAR 30 cm ion thruster, whose beam diameter is 28 cm. The technical approach here is a continuation of the "derating" technique used for the NSTAR ion thruster. With regards to the ion optics, this approach maintains low beam current densities across the ion optics to extend ion optics service life. Therefore, the 40 cm ion thruster can, at minimum, double input power and propellant throughput per thruster for the same thrust densities as the NSTAR thruster. The 40 cm thruster can further offer increased input power and propellant throughput when other grid technologies are used, such as thick-accelerator-grid (TAG) ion optics.[12]

This paper reports on the preliminary results of the development of 40 cm ion optics for the 40 cm ion thruster. Results to date include ion optics design considerations, and preliminary service life assessments and test results.

Design Considerations

Ion Thruster Performance Goals
The design goals of the 40 cm ion thruster include a 1-10 kW input power throttling range and a 550 kg xenon propellant throughput capability. Emphasis was placed on providing a flat beam profile to further improve ion optics service life.[13] This improvement occurs because several ion optics failure mechanisms are a result of the local sputter erosion of the ion optics that are a function of the local beam current density.

Ion Optics' Geometry Performance
The 40 cm ion thruster is presently envisioned to use the NSTAR ion optics aperture geometry, described in Refs. [14] and [15], and the thick-accelerator-grid geometry, described in Ref. [12]. The following analyses will focus on the use of the NSTAR geometry. Analyses with this aperture geometry allow the 40 cm thruster to take advantage of the large database of lifetime and performance data already available with this geometry.

The ion extraction capability of the 40 cm ion optics was analyzed first. Because the ion optics' aperture geometry of the NSTAR thruster was utilized, 30 cm ion optics data could be used to predict 40 cm ion optics' performance. Average beam currents per aperture (or beamlet currents) as a function of the impingement-limited total voltage for an NSTAR ion thruster are shown in Fig. 1.[11,12] The impingement-limited total voltages were defined as the voltage where the slope of the accelerator current as a function of total voltage (i.e. the sum of the absolute values of the beam and accelerator power supply voltages) was -0.02 mA/V.

3

The ion extraction capability of a given aperture geometry can be correlated to other operating conditions by utilizing a normalized perveance per hole (or NPH):

$$NPH = \frac{J'_b}{V_t^{lim\,\frac{3}{2}}} \cdot \left(\frac{l_e}{d_s}\right)^2 \qquad (1)$$

where J'_b is the beamlet current, V_t^{lim} is the impingement-limited total voltage, d_s is the screen aperture diameter, and l_e is the effective acceleration length. The effective acceleration length is defined as:

$$l_e = \sqrt{\left(l_g + t_s\right)^2 + \frac{d_s^2}{4}}, \qquad (2)$$

where l_g is the grid gap and t_s is the screen grid thickness. The impingement-limited normalized perveance per hole for the NSTAR ion optics is plotted in Fig. 2 as a function of discharge-to-total voltage ratio. As the figure demonstrates, the normalized perveance per hole is a function of the discharge-to-total voltage ratio. This effect has been noted in other studies[16,17] and can be compensated by defining a correlated normalized perveance per hole (or NPH$_{corr}$):

$$NPH_{corr} = NPH \cdot \left(\frac{V_d}{V_t^{lim}}\right)^q \qquad (3)$$

where V_d is the discharge voltage.[16] In Ref. [16], q was set to 0.2, however, a value of 1.2 was found to yield constant correlated value in this study. The correlated normalized perveance per hole for the NSTAR ion optics is also plotted in Fig. 2. As Fig. 2 shows, the correlated normalized perveance per hole is approximately 2.4×10^{-11} A/V$^{3/2}$ for the NSTAR ion optics' aperture geometry.

Total voltages for the 40 cm thruster may be determined by using the correlated normalized perveance per hole to determine the impingement-limited total voltage for a given beam current, and then adding voltage margin to the predicted limit. One selection criterion for the total voltage at a given beam current was that the total voltages provide a minimum perveance margin (i.e. the difference between the total voltage during normal operation and the impingement-limited total voltage) of at least 200 V.

High specific impulses are typically best suited for the deep space missions anticipated for the 40 cm ion thruster. This generally results in thruster operation at high R-ratios (i.e. net-to-total accelerating voltages),

and, therefore, high accelerator voltages. These high accelerator voltages are beneficial because they reduce accelerator grid erosion rates and, therefore, extend grid service life. The upper limit of the accelerator voltage is limited, however, by the onset of electron backstreaming. This electron backstreaming limit can be estimated with a semi-empirical equation derived by Kaufman for the maximum R-ratio as a function of the ion optics' aperture geometry.[18] However, since the 40 cm ion optics' aperture geometry is the same as that for the NSTAR ion optics, electron backstreaming limit data from NSTAR ion optics' tests can be used.[11,12]

The electron backstreaming limit and, therefore, the maximum R-ratio, are also functions of the peak beamlet current. This peak beamlet current is directly proportional to the peak beam current density just downstream of the ion optics, and, therefore, proportional to the beam current density divided by the beam flatness parameter (i.e. average-to-peak beam current density).[10,11] Data with the NSTAR 30 cm ion optics from Ref. [11] shows that this relation is a function of beam power supply voltage and may be nonlinear. However, the electron backstreaming can be conservatively estimated by assuming a –1 V per 1 A/m^2 dependence on the peak beam current density. The electron backstreaming limit (or V_{eb}) for the 40 cm ion thruster can, therefore, be estimated by:

$$V_{eb} = V_b \cdot \left(\frac{1 - R_{max}^0}{R_{max}^0}\right) + \frac{4 \cdot J_b}{\pi \cdot d_b^2 \cdot f_{flat}} \cdot k_{corr}. \qquad (4)$$

Here, J_b is the beam current, d_b is the beam extraction diameter, f_{flat} is the beam flatness parameter, k_{corr} is the correction for peak beam current density (i.e. –1 V per 1 A/m^2), and R_{max}^0 is a maximum R-ratio extrapolated to a zero beam current. The value for R_{max}^0 for the molybdenum 30 cm ion optics tested in Ref. [11] was determined to be 0.918. Equation (4) predicts 30 cm ion optics' electron backstreaming limits to within +15 V/-5 V.

For operation at high R-ratios, the selected accelerator voltage was determined by adding voltage margin to the predicted electron backstreaming limit.

A preliminary throttle table for the 40 cm ion thruster was developed based, in part, on the predicted performance of the ion optics' aperture geometry.[13] Results relevant to the ion optics are shown in Table 1 for operation at high R-ratios. Assumptions for these

proposed throttling points include a 24 V discharge voltage and a beam flatness parameter of 0.6. As the table shows, the lowest perveance margin was estimated to be 209 V. This value occurred at the lowest thruster input power. The lowest electron backstreaming margin (i.e. the difference between the absolute values of the accelerator voltage and electron backstreaming limit) occurred at the highest beam voltage and current and was estimated to be 40 V.

Grid Design Considerations

Dome-shaped grids, similar to those used on the NSTAR thruster, were chosen for the design of the 40 cm ion optics. This was because dome-shaped grids are naturally suited for large-area ion optics. Reasons for this included: 1) the dome shape mitigates thermally induced buckling during thruster operation, and, therefore, provides a relatively stable grid gap throughout the ion optics' area; and 2) the dome shape provides stiffness under vibration loads during launch. Furthermore, there is design heritage with this grid design at NASA GRC.

As discussed in previous sections, the NSTAR ion optics' aperture geometry was utilized for the 40 cm ion optics. As a result, the beam extraction diameter, grid thicknesses, and perforated geometries were fixed for the 40 cm grids. The only remaining, adjustable parameter was the dome height. It will be shown in the following paragraphs that selecting a dome height-to-chord radius similar to that of the NSTAR grids addressed most key issues associated with grid fabrication and thruster operation while having little impact on other issues concerning thermal expansion and launch stresses.

Fabrication Issues

The grid dome shape is hydrostatically formed, a process developed by NASA GRC in 1972,[19] and the apertures are photo-chemically etched. The primary concern regarding grid fabrication was that over-forming the 40 cm grids could result in aperture misalignment, significant residual stresses, and possibly even fracture the grid material. Since a grid is under a biaxial state of stress during forming (grid thicknesses are small enough to assume a thin-walled membrane), then the fractional change in area as a result of the forming process is the relevant parameter here. It can be shown that the area of the domed grid (or A_{dome}) is given by:

$$A_{dome} = \pi \cdot \left(h^2 + r_c^2\right), \qquad (5)$$

where h is the dome height and r_c is the radius at the dome base, or the chord radius. The fractional change in area from forming (or F_{dome}) is, therefore, given by:

$$F_{dome} = \frac{\pi \cdot \left(h^2 + r_c^2\right) - \pi \cdot r_c^2}{\pi \cdot r_c^2} = \left(\frac{h}{r_c}\right)^2. \qquad (6)$$

As the equation shows, the fractional change in area from forming is a function of the dome height-to-chord radius. Maintaining the same ratio as for the NSTAR 30 cm grids will, therefore, mitigate over-forming the 40 cm grids.

Thruster Operation Issues

Two thruster operation issues were identified for the 40 cm ion optics. These included thrust losses due to the dome shape and thermally-induced changes in the grid gap.

The thrust losses considered here are caused by the shape of the dome, which directs beamlets off-axis. The following analysis is similar to that done in Ref. [19]. The apertures of the NSTAR and 40 cm screen and accelerator grids are designed to be aligned throughout the grids' radius, with no beamlet steering to collimate the beam. As a result, beamlets are directed normal to the surface of the grids. The thrust (or T) produced by a domed grid can, therefore, be expressed as:

$$T = \sqrt{\frac{2 \cdot V_b \cdot m_i}{e}} \cdot \int_0^{2\pi} \int_0^{\theta_{max}} j_b^n \cdot \alpha \cdot F_t^n \cdot R_{dome}^2 \cdot \cos\theta \cdot \sin\theta \cdot d\theta \cdot d\phi$$

$$\ldots(7)$$

Here, V_b is the beam voltage, m_i is the ion mass and e is the electron charge. Within the double integral, θ_{max} is the maximum angle from the centerline of the grids, j_b^n is the beam current density normal to the grid surface, R_{dome} is the radius of curvature of the dome, α is the double-to-single ion current correction factor, and F_t^n is the beamlet divergence correction factor that does not account for divergence from the grid dome shape. The latter term is used to separate beam divergence due to beamlet expansion from beam divergence due to the dome shape. To simplify this analysis, it will be assumed that the beam current density normal to the grid surface and the ratio of double-to-single ion current are constant throughout the grid. The beam current density can, therefore, be reduced to the beam current divided by the area of the dome. Equation (7) can be expressed as:

$$T = \sqrt{\frac{2 \cdot V_b \cdot m_i}{e}} \cdot \alpha \cdot F_t^n \cdot \frac{J_b}{A_{dome}} \cdot \pi \cdot R_{dome}^2 \cdot \sin^2 \theta_{max} \,. \quad (8)$$

It can be shown that the last two terms in the equation above reduce to r_c^2. Using this and equation (5), equation (8) reduces to:

$$T = \sqrt{\frac{2 \cdot V_b \cdot m_i}{e}} \cdot \alpha \cdot F_t^n \cdot J_b \cdot \left[1 + \left(\frac{h}{r_c} \right)^2 \right]^{-1} \,. \quad (9)$$

As this equation shows, the thrust is a function of the dome height-to-chord radius. Maintaining the same ratio as that for the NSTAR 30 cm grids will, therefore, keep these thrust losses due to the dome shape of the grids the same for the 40 cm grids.

Grids thermally expand during thruster operation, which can change the grid gap when the grids are heated to their final operating temperatures. An analysis was conducted to compare 30 cm and 40 cm grids under thermal loads. The following simplifying assumptions were made (similar to those in Ref. [19]): 1) each grid and its mounting ring were at uniform, but different, temperatures; 2) the final shape of the heated grids is spherical; 3) both grid diameters investigated had the same temperatures and temperature distributions; and 4) there are no thermally-induced meridional stresses. The chord radius and arc length across the grids (or S) during operation are given by:

$$r_c^{hot} = r_c^{rt} \cdot \left(1 + \alpha_s \cdot \Delta T_s \right), \text{ and} \quad (10)$$

$$S^{hot} = S^{rt} \cdot \left(1 + \alpha_g \cdot \Delta T_g \right). \quad (11)$$

Here, α_s and α_g are the thermal expansion coefficients for the stiffener and grid materials, respectively, while ΔT_s and ΔT_g are the change in temperatures for the stiffeners and grids, respectively. The "rt" and "hot" superscripts denote parameter values at room temperature and temperatures during thruster operation, respectively. With equations (10) and (11), it can be shown that:

$$\arcsin \left(\frac{r_c^{rt} \cdot \left(1 + \alpha_s \cdot \Delta T_s \right)}{R_{dome}^{hot}} \right) \cdot R_{dome}^{hot} = \arcsin \left(\frac{r_c^{rt}}{R_{dome}^{rt}} \right) \cdot R_{dome}^{rt} \cdot \left(1 + \alpha_g \cdot \Delta T_g \right),$$
$$\dots (12)$$

where the radius of curvature for the heated grid is solved iteratively. Since it is known that:

$$h = R_{dome} - \sqrt{R_{dome}^2 - r_c^2} \,, \quad (13)$$

the height of the heated grid can be solved with equations (12) and (13).

Temperatures for this analysis were taken from Ref. [20] for a NASA J-Series 30 cm ion optics set operated at a discharge power of 210 W, which is similar to the NSTAR thruster at a 1.44 kW input power of and a 1.1 A beam current. Radial grid temperatures profiles were curve-fit with second order polynomial equations and integrated to determine average grid temperature changes. The thermal expansion of the grid-mounting hardware was also included in the analysis. Note that the results for the 40 cm grids would not be applicable to the same discharge power as for the 30 cm thruster, but would correspond to a much higher discharge power (and, therefore, beam current) since the 40 cm grids have a larger thermal mass. Furthermore, the temperature distribution across the grids and mounting hardware would not necessarily be the same because of the different thermal environments of the two thruster sizes. Regardless, the aforementioned assumptions are only intended to provide a comparison for the two grid diameters.

Analysis results are shown in Fig. 3, where the fraction of the hot-to-room temperature grid gap is plotted as a function of dome height-to-chord radius. The predicted fraction for the 30 cm ion optics was at the lower uncertainty limit of the measured value, indicating that the model reasonably predicts thermally-induced grid gap changes at this power level. As Fig. 3 further demonstrates, the predicted results for the 40 cm ion optics show that: 1) there is very little change in the fraction of the hot-to-room temperature grid gap over a wide range of dome height-to-chord radius ratios; and 2) the overall hot grid gap is about 2% smaller than that for the 30 cm ion optics at steady-state conditions. Because the dome height-to-chord radius ratio has little effect on the grid gap during steady state thruster operation, it is reasonable to utilize the same ratio as that for the NSTAR 30 cm grids so that fabrication issues and thrust losses are mitigated.

Launch Stress Issues
The two spacecraft launch issues examined included vibration-induced stresses and grid movement. In order to simplify the analysis, it was assumed that final shape of the grids under these stresses was spherical, which requires grid deflections to be small. Furthermore, only grid vibrations in the axial direction were examined. Since the apertures significantly weaken the perforated grid regions, these regions were analyzed. The perforated regions were assumed to have a tangential top edge support. For thin-walled spherical domes under axial loads from there own

6

mass, peak meridional and circumferential (i.e. hoop) stresses (or σ_{merid}^{max} and σ_{hoop}^{max}, respectively) are given by:[21]

$$\sigma_{merid}^{max} = \frac{n \cdot g \cdot \rho_{eff} \cdot R_{dome}}{1 + \cos(\theta_{max})}, \text{ and} \qquad (14)$$

$$\sigma_{hoop}^{max} = \frac{n \cdot g \cdot \rho_{eff} \cdot R_{dome}}{2}. \qquad (15)$$

Here, n is the number of gravities (i.e. g-load), g is the acceleration of gravity, and ρ_{eff} is the effective mass density of the grid perforated region. Note that $1 + \cos(\theta_{max}) \approx 2$ for all cases examined here, so that it can be assumed that the meridional and circumferential stresses are approximately equal. Solving equation (13) for R_{dome}, it can be shown that:

$$\sigma_{merid}^{max} \approx \sigma_{hoop}^{max} = \frac{n \cdot g \cdot \rho_{eff}}{4} \cdot r_c \cdot \frac{1 + \left(\dfrac{h}{r_c}\right)^2}{\dfrac{h}{r_c}}. \qquad (16)$$

As the above equation shows, maintaining a constant dome height-to-chord radius will still result in a stress increase proportional to the chord radius. An unchanged dome height-to-chord radius would increase meridional and circumferential stresses by about 40% for the 40 cm grids. However, increasing dome height-to-chord radius to account for the increased stresses in the 40 cm grids would worsen thruster performance. To determine the significance of these increased stresses, maximum meridional and circumferential stresses were calculated for these grids as a function of g-loading. These values were then used to determine the maximum webbing stresses[22] and compared to the yield strength of the grid material to determine if the 40 cm grids were at risk of plastic deformation under launch loads in the axial direction. The resulting maximum stresses were found to be significantly smaller than the material yield stress, even at high g-loads.

Note that this analysis omitted stresses resulting from radial motion, which should be included in any complete analysis. Unfortunately, this was beyond the scope of this initial effort.

Vibration-induced axial motion was also examined. The same assumptions as the prior analysis were made. For thin-walled spherical domes under axial loads from their own weight, the change in dome height (or ? h) is given by:[21]

$$\Delta h = \frac{n \cdot g \cdot \rho_{eff} \cdot R_{dome}^2}{E_{eff}} \cdot \left[\sin^2(\theta_{max}) + (1 + \nu_{eff}) \cdot \ln\left(\frac{2}{1 + \cos(\theta_{max})}\right) \right] \cdot$$
$$\qquad \dots (17)$$

Here, E_{eff} and ν_{eff} are the elastic modulus and Poisson's ratio, respectively, for the perforated region of the grids.[22] It can be shown that:

$$\cos(\theta_{max}) = \frac{1 - \left(\dfrac{h}{r_c}\right)^2}{1 + \left(\dfrac{h}{r_c}\right)^2}, \text{ and} \qquad (18)$$

$$\sin^2(\theta_{max}) = 1 - \left[\frac{1 - \left(\dfrac{h}{r_c}\right)^2}{1 + \left(\dfrac{h}{r_c}\right)^2}\right]^2. \qquad (19)$$

Both equations are merely functions of the initial dome height-to-chord radius. Solving equation (13) for R_{dome}, equation (17) can be given:

$$\Delta h = \frac{n \cdot g \cdot \rho_{eff} \cdot k}{E_{eff}} \cdot r_c^2 \cdot \left[\frac{\left[1 + \left(\dfrac{h}{r_c}\right)^2\right]^2}{2 \cdot \dfrac{h}{r_c}}\right], \qquad (20)$$

where:

$$k = \sin^2(\theta_{max}) + (1 + \nu_{eff}) \cdot \ln\left(\frac{2}{1 + \cos(\theta_{max})}\right). \qquad (21)$$

As equations (18)-(21) show, maintaining a constant dome height-to-chord radius will still result in a change in dome height proportional to the chord radius squared. Maintaining a constant dome height-to-chord radius would, therefore, approximately double grid movement for the 40 cm grids. If this grid movement is large enough, the grids could make contact under vibration loads. This occurrence, however, is not necessarily detrimental to the grids. Both the NSTAR 30 cm grids and 50 cm were found to make contact under vibration loads without detrimental effects.[23,24] As a result, this is not expected to be an issue for the 40 cm grids.

Preliminary Service Life Assessment

A preliminary service life assessment was conducted to determine the lifetime gain by utilizing 40 cm ion optics. Service life analyses included sputter erosion of

the downstream surface (i.e. pits and grooves) and aperture walls of the accelerator grid, shown in Fig. 4, and sputter erosion of the upstream surface of the screen grid.

Accelerator Grid

Accelerator grid erosion is caused by charge-exchange ions created both upstream and downstream of the neutralization plane that bombard the accelerator grid. Accelerator grid erosion from direct impingement of beam ions is assumed to be negligible here. Charge-exchange ions created upstream of the neutralization plane sputter-erode both the aperture walls and the downstream surface of the accelerator grid, while those created downstream of the neutralization plane only sputter-erode the downstream surface (see Fig. 4). This assertion has been demonstrated, in part, by several numerical models.[25-28] It was also verified via testing where a two-grid system that was tested at high background pressures exhibited excessive pit and groove erosion of the downstream accelerator grid but little accelerator aperture enlargement.[29,30]

The volumetric erosion rate in the region of a single accelerator grid aperture (or $\dot{V}'_{accel}$) can be expressed as:

$$\dot{V}'_{accel} = \left(\dot{V}'^{up}_w + \dot{V}'^{up}_{p-g}\right) + \dot{V}'^{dwn}_{p-g} . \quad (22)$$

Here, $\dot{V}'_w$ and $\dot{V}'_{p-g}$ are the volumetric erosion rates of the aperture walls and pit and groove erosion, respectively, in the region of an aperture. The "up" and "dwn" superscripts denote that charge-exchange ions were created upstream and downstream of the neutralization plane, respectively. The variables in this equation can be expressed as:

$$\dot{V}'^{up}_w + \dot{V}'^{up}_{p-g} = \frac{J'^{up}_i}{e \cdot \rho_a} \cdot \frac{m^a_{amu}}{N_A} \cdot Y \cdot f^h_{corr} , \text{ and} \quad (23)$$

$$\dot{V}'^{dwn}_{p-g} = \frac{J'^{dwn}_i}{e \cdot \rho_a} \frac{m^a_{amu}}{N_A} \cdot Y \cdot f^{p-g}_{corr} . \quad (24)$$

Here, J'_i is the impingement current per aperture, m^a_{amu} is the atomic mass of the accelerator grid material, ρ_a is the mass density of the accelerator grid, e is the electronic charge, N_A is Avogadro's number, Y is the grid sputter yield for an orthogonal angle of incidence, and f_{corr} is a sputter yield correction factor. This correction factor accounts for non-orthogonal angle-of-incidence sputtering, variations in ion sputtering energies, re-deposition of sputtered material, and any other sputtering phenomena that can affect volumetric

sputter erosion. Note that the prime superscripts denote parameter values per aperture. The aforementioned equations could be expressed without the prime superscripts to define the volumetric erosion rates for the entire accelerator grid.

All of the above variables are known except for the impingement currents per aperture and the sputter yield correction factors. These impingement currents are from charge-exchange ions created both upstream and downstream of the neutralization plane. These currents will be determined here as was done by Monheiser and Wilbur,[31,32] but with some modifications. The charge-exchange ion production current per aperture is given by:

$$J'^{up}_i = J'_b \cdot \sigma_{c-e} \cdot \int_{l_{up}}^{l_n} n_n \cdot dz , \text{ and} \quad (25)$$

$$J'^{dwn}_i = J'_b \cdot \sigma_{c-e} \cdot \int_{l_n}^{\infty} F_g \cdot n_b \cdot dz . \quad (26)$$

Here, J'_b is the beamlet current, σ_{c-e} is the charge-exchange cross-section, n_n is the neutral density distribution upstream of the neutralization plane from discharge chamber neutrals, n_b is the vacuum facility background neutral density, z is the axial dimension, l_{up} is the upstream location of the potential well that traps charge-exchange ions in this region, and l_n is the neutralization length. F_g is the accelerator grid view factor for a charge-exchange ion created downstream of the neutralization, and, therefore, represents the probability that a charge-exchange created in this region will impinge the accelerator grid. The assumptions for equation (26) include, in part: 1) potential gradients in the downstream beam plasma are too small to divert charge-exchange ions; and 2) the facility background neutral density has isotropic velocity distribution.

Equations (25) and (26) differ from those derived by Monheiser and Wilbur in the following ways. First, the integral in equation (25) has l_{up} as the upstream limit and not the accelerator grid downstream surface. This is because this upstream axial location more accurately defines those charge-exchange ions trapped in this region by the electrode potential gradients. Second, the integral in equation (25) does not include the contribution of the facility background neutral density. This simplifying assumption is valid if background facility pressures are kept low. This appeared to be the

case for the NSTAR thruster operated at NASA GRC's Vacuum Facility 5, where comparisons of accelerator currents produced in this facility to those produced on the Deep Space 1 spacecraft were within 0.4 mA (e.g. less than 10% of the total impingement at 2 kW).[2] Finally, the contribution of neutrals escaping the discharge chamber downstream of the neutralization plane were omitted in equation (26). This is because these neutrals do not have an isotropic velocity distribution, but a velocity distribution directed away from the accelerator grids, and, therefore, should be omitted.

It will be assumed here, as was done by Monheiser and Wilbur,[31,32] that the neutral density distribution along the axis of an aperture can be approximated by the discharge chamber neutral density, n_d, multiplied by a distribution function, $N(z)$, so that:

$$\int_{l_{up}}^{l_n} n_n \cdot dz \approx n_d \cdot \int_{l_{up}}^{l_n} N(z) \cdot dz , \qquad (27)$$

where $N(z)$ is only a function of the ion optics' aperture geometry. Furthermore, the same one-dimensional view factor utilized by Monheiser and Wilbur will be used here. Equations (25) and (26) can, therefore, be re-written as:

$$J_i'^{up} = J_b' \cdot \sigma_{c-e} \cdot n_d \cdot \int_{l_{up}}^{l_n} N(z) \cdot dz , \text{ and} \qquad (28)$$

$$J_i'^{dwn} = \frac{J_b' \cdot \sigma_{c-e} \cdot n_b}{2} \cdot \left[\sqrt{\frac{d_b^2}{4} + l_n^2} - l_n \right], \qquad (29)$$

where d_b is the beam extraction diameter. It can be shown that $l_n << d_b$, so that equation (29) can be expressed as:

$$J_i'^{dwn} = \frac{J_b' \cdot \sigma_{c-e} \cdot n_b \cdot d_b}{4} . \qquad (30)$$

Because equation (30) utilizes a one-dimensional view factor approximation, it will only accurately predict impingement current contributions for apertures at the accelerator grid center, assuming small beamlet divergence half-angles. Equation (30) over-predicts impingement current contributions for apertures radially away from the accelerator grid center. Equation (30) also over-predicts impingement currents because potential gradients in the beam plasma were assumed to be too small to divert charge-exchange ions from the accelerator grid. Plasma potential measurements in NSTAR thrusters have demonstrated that there are radial and axial potential gradients.[3,33]

Although these voltage gradients are only on the order of a few volts, charge-exchange ions produced in this region have significantly lower energies and can, therefore, be directed away from the grids.

The discharge chamber neutral density is determined by:

$$n_d = \frac{\left(1 - \eta_d^{++}\right) \cdot \dot{m}_d}{\varphi \cdot d_b^2 \cdot \sqrt{\dfrac{\pi \cdot m_n \cdot k_B \cdot T_n}{32}}} . \qquad (31)$$

Here, η_d^{++} is the discharge chamber propellant utilization efficiency accounting for doubly charged ions, $\dot{m}_d$ is the discharge chamber flow rate, φ is the ion optics' neutral transparency, m_n is propellant atomic mass, k_B is Boltzmann's constant, and T_n is the neutral propellant temperature.

Because charge-exchange production is a direct function of beamlet current, the peak beamlet current is necessary for determining the maximum local sputter erosion rate of the accelerator grid. This peak beamlet current is given by:

$$J_b'^{pk} = \left(\frac{d_a}{d_b} \right)^2 \cdot \frac{J_b}{f_{flat} \cdot F_{oa}^a} , \qquad (32)$$

where d_a is the accelerator aperture diameter, J_b is the beam current, and F_{oa}^a is the open area fraction of the accelerator grid.

Equations (31) and (32) can be combined with equation (28) to yield:

$$J_i'^{up-pk} = \frac{d_a^2}{d_b^4} \cdot \frac{J_b}{f_{flat} \cdot F_{oa}^a} \cdot \sigma_{c-e} \cdot \frac{\left(1 - \eta_d^{++}\right) \cdot \dot{m}_d}{\varphi \cdot \sqrt{\dfrac{\pi \cdot m_n \cdot k_B \cdot T_n}{32}}} \cdot \int_{l_{up}}^{l_n} N(z) \cdot dz \cdot$$

$$\dots (33)$$

This equation can be used with equation (23) to define this peak volumetric sputter erosion rate per aperture. This is because the ion flux from this equation will impinge the aperture region within which it was created. However, the impingement current in equation (30) can impinge on any pit-and-groove site on the accelerator grid. It is, therefore, more convenient to utilize an average beamlet current for equation (30). The resulting impingement current can be expressed as:

$$J_i'^{dwn-avg} = \frac{J_b \cdot \sigma_{c-e} \cdot n_b \cdot d_a^2}{4 \cdot d_b \cdot F_{oa}^a} . \qquad (34)$$

9

The effect of beam extraction diameter on accelerator grid volumetric erosion rates can now be assessed. Comparisons are made at the same operating electrode voltages, beam currents, and discharge chamber flow rates, so that the relative effects of beam extraction diameter can be determined. Because the ion optics' aperture geometry is unchanged, a peak volumetric erosion rate per aperture ratio can be established for charge-exchange ions produced upstream of the neutralization plane, where:

$$\frac{\dot{V}_w'^{up} + \dot{V}_{p-g}'^{up}}{\left(\dot{V}_w'^{up} + \dot{V}_{p-g}'^{up}\right)^{NSTAR}} = \left(\frac{d_b^{NSTAR}}{d_b}\right)^4 \cdot \frac{f_{flat}^{NSTAR}}{f_{flat}} \cdot \frac{\left(1-\eta_d^{++}\right)}{\left(1-\eta_d^{++NSTAR}\right)} \cdot$$
$$\ldots(35)$$

Here, the "NSTAR" superscripts denote parameters for the NSTAR 30 cm ion thruster. Note that equation (35) assumes that changes in l_{up} and l_n do not affect the neutral density distribution integral in equation (28). It can be shown that this is likely the case for l_n due to the long neutralization plane lengths and the exponential decay of neutral density downstream of an accelerator aperture. Although comparisons are made for the same ion optics' geometries and electrode voltages, it is presently unclear what the exact effect the varying beamlet current (and, therefore, varying space-charge) will have on l_{up}.

An average volumetric erosion rate per aperture ratio can further be established for charge-exchange ions produced downstream of the neutralization plane, where:

$$\frac{\dot{V}_{p-g}'^{dwn}}{\dot{V}_{p-g}'^{dwn\,NSTAR}} = \frac{d_b^{NSTAR}}{d_b} \cdot \tag{36}$$

It is assumed that background neutral densities are independent of beam extraction diameter, which is reasonable because discharge chamber flow rates are assumed unchanged.

The results of equations (35) and (36) are shown in Fig. 5. In this figure, the discharge chamber propellant utilization efficiencies and flatness parameters were assumed to be the same for all beam extraction diameters. As Fig. 5 demonstrates, increasing the NSTAR thruster beam extraction diameter to 40 cm reduces peak volumetric erosion rates by charge-exchange ions originating upstream of the neutralization plane by a factor of 0.25, or by 75%. This is expected since the number of accelerator apertures available for erosion was doubled and the

discharge chamber neutral density available for charge-exchange production was halved.

The 40 cm beam diameter further reduces average volumetric erosion rates by charge-exchange ions originating downstream of the neutralization plane by a factor of 0.7, or about 30%. This occurs because although the downstream accelerator grid surface area available for sputter erosion doubled for the 40 cm thruster, its view factor for downstream charge-exchange ions increased by a factor directly proportional to the 40 cm-to-30 cm ion optics diameter ratio.

The service life enhancement due these reduced erosion rates requires knowledge of which impingement current (i.e equation (28) or (30)) is more dominant. It may be possible to gain insight into the relative magnitude of each impingement current through short-term testing, which is the topic of Appendix A. However, a rough estimate of the improvement in accelerator grid propellant throughput capability may be made for the 40 cm ion optics if it is assumed that operating conditions are the same as those of the NSTAR thruster. Two accelerator grid failure mechanisms are considered separately.

The first failure mechanism considered is electron backstreaming due to accelerator grid aperture enlargement. Since an ongoing life test of an NSTAR ion thruster has successfully processed about 140 kg of xenon, it will be conservatively assumed that this 140 kg is the propellant throughput capability of the NSTAR ion optics with regards to electron backstreaming. Upstream of the neutralization plane, it is assumed that the fraction of charge-exchange ions that sputter-erode the aperture walls (as opposed to those that erode the downstream surface) is either constant or decreases with a decreasing beamlet current. This assumption is reasonable since NSTAR wear test results have shown that aperture wall mass loss due to sputter erosion exhibited a smaller flatness parameter (i.e. average mass loss per unit grid area divided by the peak mass loss per unit grid area) than the beam flatness parameter.[3,34] As a result, the ratio of accelerator aperture wall volumetric erosion rate per hole of the 40 cm thruster to that of the NSTAR thruster is equal to equation (35). Assuming that discharge chamber propellant utilization efficiencies and beam flatness parameters are the same for both thrusters, the 40 cm thruster offers a 4x increase in

propellant throughput. The propellant throughput capability of the 40 cm thruster is, therefore, estimated to be about 560 kg for this failure mechanism, which exceeds the goal of 550 kg.

The second failure mechanism considered is structural failure of the grid due to the pit and groove erosion of the downstream surface of the accelerator grid. The failure criterion here is assumed to be groove erosion through 80% of the grid thickness. Pit erosion is not considered because erosion through the grid thickness does not compromise the structural integrity of the grid. Past analyses based on NSTAR thruster wear test results estimated a propellant throughput capability of the NSTAR thruster of about 410 kg for this failure mechanism.[9] If it is conservatively assumed that charge-exchange ions created downstream of the accelerator grid dominate groove erosion, then the 40 cm offers a 1.4x increase in propellant throughput capability. The propellant throughput capability of the 40 cm thruster is, therefore, estimated to be about 570 kg for this failure mechanism, which exceeds the goal of 550 kg.

The propellant throughput capability of the 40 cm thruster is estimated to be about 560 kg for electron backstreaming and 570 kg for a structural failure. The 40 cm thruster is, therefore, anticipated to meet the propellant throughput goal of 550 kg of xenon. (Note that these preliminary results are rough estimates subject to the assumptions made for the calculations.) A more accurate service life assessment requires that detailed analyses be made at the anticipated operating conditions for the 40 cm ion thruster.

Screen Grid
Screen grid erosion is caused by discharge chamber ions that sputter erode the upstream surface of the screen grid. This sputter erosion generally causes a chamfering of the screen grid apertures. Failure occurs when the screen grid erosion results in the removal of the screen grid webbing, allowing beam ions to directly impinge on the accelerator grid. NSTAR thruster life testing indicated that screen grid erosion was peaked at the center on the grid.[3] This is expected since the center of the grid is where the radial beam current density, and discharge ion current density just upstream of the ion optics, is highest.

Discharge chamber particles that sputter-erode the screen grid include both singly and doubly charged ions. The screen grid is at discharge cathode potential and the discharge chamber plasma is typically assumed to be at the discharge anode potential. As a result, singly charged ions are assumed to have energies equivalent to the discharge voltage while doubly charged ions have twice the discharge voltage. The volumetric erosion rate in the region of a single screen grid aperture (or $\dot{V}'_s$) can be defined as:

$$\dot{V}'_s = \frac{J'^+_s}{e \cdot \rho_s} \cdot \frac{m^s_{amu}}{N_A} \cdot Y^+ \cdot f^{s+}_{corr} + \frac{J'^{++}_s}{2 \cdot e \cdot \rho_s} \cdot \frac{m^s_{amu}}{N_A} \cdot Y^{++} \cdot f^{s++}_{corr} \cdot$$

$$\dots(37)$$

Here, J'_s is the screen grid current per aperture, m^s_{amu} is the atomic mass of the screen grid material, ρ_s is the mass density of the screen grid, and f^s_{corr} is a sputter yield correction factor, similar to that used in the previous section. The "+" and "++" superscripts denote parameter values for the singly and doubly charged discharge chamber ions, respectively.

Note that NASA xenon ion thrusters are typically operated at discharge voltages of about 25 V, which is a part of the derated approach. As a result, singly charged ions have energies on the order of the sputter yield threshold energies.[35] Furthermore, sputter yields increase exponentially with ion energy at these low discharge voltages. Because the ratio of doubly-to-singly charged ion current ranges between 0.05 to 0.25 for the NSTAR ring-cusp discharge chamber,[3] it is reasonable to assume that doubly charged ions dominate screen grid erosion for these thrusters. Equation (37) can, therefore, be rewritten as:

$$\dot{V}'_s \approx \frac{J'^{++}_s}{2 \cdot e \cdot \rho_s} \cdot \frac{m^s_{amu}}{N_A} \cdot Y^{++} \cdot f^{s++}_{corr} \cdot \quad (38)$$

Because screen grid erosion is highest at the center of the grid, a peak current is necessary for determining the maximum local sputter erosion rate of the screen grid in equation (38). It can be shown that this peak, doubly charged screen grid current per aperture is given by:

$$J'^{++pk}_s = \frac{1-\phi_i}{\phi_i} \cdot \left(\frac{d_s}{d_b}\right)^2 \cdot \frac{J_b}{f_{flat} \cdot F^s_{oa}} \cdot \frac{R_j}{1+R_j} \cdot \quad (39)$$

Here, ϕ_i is the screen grid transparency to discharge ions, d_s is the screen grid aperture diameter, F^s_{oa} is the screen grid open area fraction, and R_j is the ratio of doubly-to-singly charged ion current. Note that equation (39) assumes that R_j is constant throughout the beam. Equation (39) can be plugged into equation

(38) to determine a peak screen grid volumetric erosion rate per aperture.

The effect of beam extraction diameter on the peak screen grid volumetric erosion rate can now be assessed. Comparisons are made at the same operating discharge voltages, total voltages, and beam currents so that the relative effects of beam extraction diameter can be determined. Because the ion optics aperture geometry is unchanged, a peak screen grid volumetric erosion rate per aperture ratio can be established:

$$\frac{\dot{V}_s'}{\dot{V}_s'^{NSTAR}} = \frac{\dfrac{1-\phi_i}{\phi_i}}{\dfrac{1-\phi_i^{NSTAR}}{\phi_i^{NSTAR}}} \cdot \left(\frac{d_b^{NSTAR}}{d_b}\right)^2 \cdot \frac{f_{flat}^{NSTAR}}{f_{flat}} \cdot \frac{\dfrac{R_j}{1+R_j}}{\dfrac{R_j^{NSTAR}}{1+R_j^{NSTAR}}} \cdot$$

$$\dots(40)$$

The results of equation (40) are shown in Fig. 6. In this figure, the screen grid discharge ion transparencies, ratio of doubly-to-singly charged ion currents, and flatness parameters were assumed to be constant for all beam extraction diameters. The screen grid discharge ion transparency assumption is conservative because this ion transparency is known to increase with decreasing beam current densities, which can be inferred from data in Refs. [11] and [12]. As Fig. 6 demonstrates, increasing the NSTAR thruster beam extraction diameter to 40 cm reduces peak screen grid volumetric erosion rates by a factor of 0.5, or by 50%. This is expected since the amount of screen grid webbing available for erosion was doubled.

The service life of the 40 cm thruster is assumed to be double that of the NSTAR screen grid, given the aforementioned assumptions. NSTAR wear test results showed that screen grid erosion was minimal after processing 88 kg of xenon.[3] From these results, the NSTAR screen grid was estimated to have a 460 kg propellant throughput capability utilizing a conservative failure criterion of sputter erosion through half of the screen grid thickness.[9] The 40 cm thruster is, therefore, anticipated to be capable of processing about 920 kg of xenon, which exceeds the goal of 550 kg.

Preliminary Results

Fabrication of 40 cm Ion Optics
One 40 cm ion optics' set has been successfully fabricated to date, and is shown in Fig. 7 with 30 cm ion optics for comparison. The dome height-to-chord radius was matched to that of the NSTAR 30 cm ion optics. Additional ion optics' sets are presently being fabricated. These additional optics' sets not only include the NSTAR aperture geometry, but also a thick-accelerator-grid (i.e. TAG) aperture geometry for further improvements in accelerator grid service life.[12]

Preliminary Tests

Test Hardware
Preliminary performance tests were conducted on a laboratory model 40 cm ion thruster, described in Ref. [13]. Because 40 cm ion optics were unavailable for these initial tests, 50 cm ion optics from a prior NASA program were used.[24] These ion optics had an ion optics' aperture geometry similar to the NSTAR geometry, with two differences. First, the grid gap was 15% larger than the nominal NSTAR gap at the grid center and 8-33% larger at mid-radius. Second, the accelerator grid thickness was 25% thinner than the nominal NSTAR grid thickness.

A power console similar to that described in Ref. [36] powered the thruster. This power console was modified to allow the thruster to be throttled up to 10 kW. During the tests reported herein, neutralizer common was electrically tied to facility ground. A high purity gas feed system was used to provide xenon to the discharge cathode, discharge chamber, and neutralizer through separate mass flow controllers. Testing was conducted in Vacuum Facility 11 at NASA GRC. This 2.2 m diameter × 7.9 m long facility is evacuated with seven cryogenic pumps and a turbomolecular pump. The total measured facility pumping speed was greater than 100,000 l/s with xenon.

During thruster operation, voltages and currents were measured with digital multimeters and xenon flows with mass flow meters. Beam current density profiles were measured with a planar probe mounted onto a two-axis probe motion system. Both the probe and two-axis probe motion system are described in detail in Refs. [11] and [12]. The planar probe of this study had an exposed surface area of 0.25 cm^2.

Test Results
The two measurements reported below include impingement-limited total voltages and radial beam current density profiles. Although accelerator currents

and electron backstreaming limits were measured, high background pressures, the larger-than-nominal cold grid gap, and the smaller-than-nominal accelerator grid thickness made comparisons with NSTAR ion optics' data difficult. Impingement-limited total voltages were determined from plots of accelerator current as a function of total voltage where the slope was -0.02 mA/V. Uncertainties in impingement-limited total voltage determinations (and, therefore, perveance margins) were within ±10 V. All radial beam current density profiles were measured 49 mm downstream of the geometric center of the accelerator grid.

Impingement-limited total voltages were measured at beam currents of 1.20, 2.70, 3.52, and 4.75 A. Although impingement-limited total voltages for this ion optics' set were decreasing with accumulated operation, there was no attempt to burn-in this optics' set prior to collecting the data presented in this paper.[11,12] As a result, perveance data are conservative and, therefore, preliminary. The resulting average beamlet currents as a function of the impingement-limited total voltage are plotted in Fig. 8 with NSTAR ion optics' data for comparison. As Fig. 8 shows, impingement-limited total voltages for the 40 cm thruster were 150-210 V higher than those of the NSTAR thruster ion optics. This is expected given the larger cold grid gap of the ion optics used on the 40 cm thruster. Although the accelerator grid used on the 40 cm thruster was thinner than that of the NSTAR thruster, accelerator grid thickness has been shown to have a negligible effect on perveance.[12,37,38]

To permit comparisons between these 40 cm thruster data and the NSTAR ion optics' data, the 40 cm thruster impingement-limited total voltages were corrected for an NSTAR grid gap. This was done by using equation (1) to determine a normalized perveance per hole at a given beam current, and then using this value to determine a new impingement-limited total voltage for an effective acceleration length equal to that of the NSTAR ion optics. These corrected results are also plotted in Fig. 8. As the figure shows, corrected impingement-limited total voltages for the 40 cm thruster were less than 50 V higher than those of the NSTAR thruster ion optics.

The mean value of the correlated normalized perveance per hole for the ion optics of the 40 cm thruster was 1.8×10^{-11} A/V$^{3/2}$, which is 25% lower than the 2.4×10^{-11} A/V$^{3/2}$ measured for the 30 cm NSTAR

ion optics. The cause for this difference is presently unknown. Regardless, the 40 cm thruster with the 50 cm ion optics was able to successfully operate at the lowest total voltages in Table 1 for all beam currents tested, albeit with a reduced perveance margin.

Radial beam current density profiles at beam currents of 1.20, 2.70, 3.52, and 4.75 A are shown in Fig. 9. Beam power supply and accelerator voltages were those corresponding to the minimum total voltages for each beam current listed in Table 1. Although the beam current density profiles exhibited a repeatable, slightly irregular profile within a 150 mm radius, there was no substantial peak in the profile center as with the NSTAR 30 cm ion thruster.[10-12]

Conclusions

A 40 cm ion thruster is being developed at the NASA GRC to obtain input power and propellant throughput capabilities of 10 kW and 550 kg, respectively. This engine has twice the beam area as the NSTAR thruster, whose beam diameter is 28 cm. The technical approach here is a continuation of the "derating" technique used for the NSTAR ion thruster. With regards to the ion optics, this approach maintains low beam current densities across the ion optics to extend ion optics service life. The 40 cm thruster can further offer increased input power and propellant throughput when other grid technologies are used, such as thick-accelerator-grid (TAG) ion optics.

The 40 cm ion thruster utilizes the NSTAR ion optics aperture geometry to take advantage of the large database of lifetime and performance data already available. The ion extraction capability and electron backstreaming limits of the 40 cm ion optics were, therefore, be estimated by utilizing NSTAR 30 cm ion optics data.

A preliminary throttle table for the 40 cm ion thruster was developed based, in part, on the predicted performance of the ion optics' aperture geometry. The lowest perveance margin was estimated to be 209 V and occurred at the lowest thruster input power. The lowest electron backstreaming margin was estimated to be 40 V and occurred at the highest beam voltage and current.

Dome-shaped grids were chosen for the design of the 40 cm ion optics because they are naturally suited for

large-area ion optics. A dome height-to-chord radius ratio similar to that of the NSTAR grids was further utilized because it addressed most key issues associated with grid fabrication and thruster operation while having little impact on other issues concerning thermal expansion and launch stresses.

A preliminary service life assessment was conducted to determine the lifetime gain by utilizing larger area ion optics. Utilizing long duration test results with NSTAR ion optics, comparisons indicated that the propellant throughput goal of 550 kg of xenon is possible with 40 cm ion optics utilizing the NSTAR ion optics geometry.

One 40 cm ion optics' set has been successfully fabricated to date. Additional ion optics' sets are presently being fabricated.

Preliminary performance tests were conducted on a laboratory model 40 cm ion thruster. Because 40 cm ion optics were not available for these initial tests, 50 cm ion optics were used. These ion optics had a cold gap that was 8-33% larger than that of the NSTAR ion optics geometry. Impingement-limited total voltages were measured at beam currents of 1.20, 2.70, 3.52, and 4.75 A. The 40 cm thruster with the 50 cm ion optics was able to successfully operate at the lowest predicted total voltages for all beam currents tested. Impingement-limited total voltages corrected for their larger cold grid gap for the 40 cm thruster were less than 50 V higher than those of the NSTAR thruster ion optics.

References

[1] Rawlin, V.K., et al. "An Ion Propulsion System for NASA's Deep Space Missions," AIAA Paper 99-4612, September 1999.

[2] Polk, J.E., et al., "In-Flight Performance of the NSTAR Ion Propulsion System on the Deep Space One Mission," IEEE Aerospace Conference Paper 8.0304, March 2000.

[3] Polk, J.E., et al., "An Overview of the Results from an 8200 Hour Wear Test of the NSTAR Ion Thruster," AIAA Paper 99-2446, June 1999.

[4] Anderson, J.R., et al., "Performance Characteristics of the NSTAR Ion Thruster During an On-going Long Duration Ground Test," IEEE Aerospace Conference Paper 8.0303, March 2000.

[5] Personal Communication, Anderson, J.R., Jet Propulsion Laboratory, Pasadena, CA, May 2001.

[6] Rawlin, V.K., "Erosion Characteristics of Two-Grid Ion Accelerating Systems," IEPC Paper 93-175, September 1993.

[7] Brophy, J.R., Polk, J.E., and Rawlin, V.K., "Ion Engine Service Life Validation by Analysis and Testing," AIAA Paper 96-2715, July 1996.

[8] Patterson, M.J., et al., "Ion Propulsion Development Activities at NASA Glenn Research Center," AIAA Paper 2000-3810, July 2000.

[9] Soulas, G.C., "Grid Technology Analyses for CNSR," Presentation at NASA Glenn Research Center, January 2000.

[10] Soulas, G.C., Foster, J.E., and Patterson, M.J. "Performance of Titanium Optics on a NASA 30 cm Ion Thruster," AIAA Paper 00-3814, July 2000.

[11] Soulas, G.C., "Performance Evaluation of Titanium Ion Optics for the NASA 30 cm Ion Thruster," IEPC Paper 01-092, October 2001.

[12] Soulas, G.C., "Improving the Total Impulse Capability of the NSTAR Ion Thruster with Thick-Accelerator-Grid Ion Optics," IEPC Paper 01-081, October 2001.

[13] Patterson, M.J., et al., "Development Status of a 5/10-kW Class Ion Engine," AIAA Paper 2001-3489, July 2001.

[14] Christensen, J.A., et al., "Design and Fabrication of a Flight Model 2.3 kW Ion Thruster for the Deep Space 1 Mission," AIAA Paper 98-3327, July 1998.

[15] Sovey, J.S., et al., "Development of an Ion Thruster and Power Processor for New Millenium's Deep Space 1 Mission," AIAA Paper 97-2778, December 1997.

[16] Aston, G., Kaufman, H.R., and Wilbur, P.J. "Ion Beam Divergence Characteristics of Two-Grid Accelerator Systems," AIAA Journal, vol. 16, no. 5, May 1978, pp. 516-524.

[17] Rawlin, V.K., "Characterization of Ion Accelerating Systems on NASA LeRC's Ion Thrusters," AIAA Paper 92-3827, July 1992.

[18] Kaufman, H.R., "Technology of Electron Bombardment Ion Thrusters," Advances in Electronics and Electron Physics, vol. 36, Academic Press, Inc., New York, 1974, pp. 265-373.

[19] Rawlin, V.K., Banks, B.A., and Byers, D.C., "Design, Fabrication, and Operation of Dished

Accelerator Grids on a 30-cm Ion Thruster," AIAA Paper 72-486, April 1972.

[20] MacRae, G.S., Zavesky, R.J., and Godder, S.T., "Structural and Thermal Response of 30 cm Diameter Ion Thruster Optics," AIAA Paper 89-2719, July 1989.

[21] Young, W.C., <u>Roark's Formulas for Stress and Strain</u>, 6th Ed., McGraw Hill, New York, 1989, p. 523.

[22] Horvay, G., "The Plane-Stress Problem of Perforated Plates," Journal of Applied Mechanics, September 1952, pp. 355-360.

[23] Personal Communication, Rawlin, V.K., NASA Glenn Research Center, Cleveland, OH, August 2001.

[24] Rawlin, V.K. and Millis, M.G., "Ion Optics for High Power 50-cm-diam Ion Thrusters," AIAA Paper 89-2717, July 1989.

[25] Whealton, J.H., Kirkman, D.A., and Raridon, R.J., "Electrostatic Ion Thruster Optics Calculations," AIAA Paper 92-3830, July 1992.

[26] Peng, X., Ruyten, W.M., and Keefer, D., "Further Study of the Effect of the Downstream Plasma Condition on Accelerator Grid Erosion in an Ion Thruster," AIAA Paper 92-3829, July 992.

[27] Peng, X., Ruyten, W.M., and Keefer, D., "Charge-Exchange Grid Erosion Study for Ground-Based and Space-Based Operations of Ion Thrusters," IEPC Paper 93-173, September 1993.

[28] Arakawa, Y. and Nakano, M., "An Efficient Three-Dimensional Optics Code for Ion Thruster Research," AIAA Paper 96-3198, July 1996.

[29] Brophy, J.R., Polk, J.E., and Pless, L.C., "Test-to-Failure of a Two-Grid, 30-cm Dia. Ion Accelerator System," IEPC Paper 93-172, September 1993.

[30] Polk, J.E., Brophy, J.R., and Wang, J., "Spatial and Temporal Distribution of Engine Accelerator Grid Erosion," AIAA Paper 95-2924, July 1995.

[31] Monheiser, J.M., and Wilbur, P.J., "Effects of Design and Operating Conditions on Accelerator Grid Impingement Current," IEPC Paper 93-174, September 1993.

[32] Monheiser, J.M., and Wilbur, P.J., "Development and Verification of a Model to Predict Impingement Currents for Ion Thrusters," NASA Contractor Report CR-195322, April 1994.

[33] Foster, J.E., Soulas, G.C., and Patterson, M.J., "Plume and Discharge Plasma Measurements of an NSTAR-type Ion Thruster," AIAA 2000-3812, July 2000.

[34] Polk, J.E., et al., "The Effect of Carbon Deposition on Accelerator Grid Wear Rates in Ion Engine Ground Testing," AIAA Paper 2000-3662, July 2000.

[35] Stuart, R.V. and Wehner, G.K., "Sputter Yields at Very Low Bombarding Ion Energies," <u>Journal of Applied Physics</u>, vol. 33, no. 7, July 1962, pp. 2345-2352.

[36] Pinero, L.R., Patterson, M.J., and Satterwhite, V.E., "Power Console Development for NASA's Electric Propulsion Outreach Program," IEPC Paper 93-250, September 1993.

[37] Rawlin, V.K., "Performance of 30-cm Ion Thrusters with Dished Accelerator Grids," AIAA Paper 73-1053, October-November 1973.

[38] Rovang, D.C. and Wilbur, P.J., "Ion Extraction Capabilities of Two-Grid Accelerator Systems," IEPC Paper 84-86, July 1984.

Appendix A

Accurately assessing the accelerator grid service life enhancement with 40 cm ion optics requires knowing whether charge-exchange ions created upstream or downstream (i.e equation (28) or (30), respectively) of the neutralization plane dominate the total impingement current. It may be possible to gain insight into the relative magnitude of each impingement current by comparing impingement currents of both 30 and 40 cm ion optics at similar operating conditions. Total impingement currents can be determined for equations (28) and (30) by replacing the beamlet current with the beam current, to yield:

$$J_i^{up} = J_b \cdot \sigma_{c-e} \cdot \frac{\left(1 - \eta_d^{++}\right) \cdot \dot{m}_d}{d_b^2 \cdot \varphi \cdot \sqrt{\dfrac{\pi \cdot m_n \cdot k_B \cdot T_n}{32}}} \cdot \int_{l_{up}}^{l_n} N(z) \cdot dz,$$

$$\text{...and} \quad (A1)$$

$$J_i^{dwn} = \frac{J_b \cdot \sigma_{c-e} \cdot n_b \cdot d_b}{4}. \qquad (A2)$$

Because the $N(z)$ and l_{up} are unknown, solving for the value of each current is not possible. However, impingement current ratios can be used to determine the relative magnitude of each term as a function of beam extraction diameter. Using the same assumptions as with equations (35) and (36), it can be shown that:

15

$$\frac{J_i^{up}}{J_i^{up\ NSTAR}} = \left(\frac{d_b^{NSTAR}}{d_b}\right)^2 \cdot \frac{f_{flat}^{NSTAR}}{f_{flat}} \cdot \frac{\left(1-\eta_d^{++}\right)}{\left(1-\eta_d^{++\ NSTAR}\right)},$$
$$\dots \text{and (A3)}$$

$$\frac{J_i^{dwn}}{J_i^{dwn\ NSTAR}} = \frac{d_b}{d_b^{NSTAR}}. \qquad (A4)$$

Equations (A3) and (A4) show that if 40 cm thruster accelerator currents are greater than those for the NSTAR thruster at similar operating conditions (assuming similar flatness parameters and discharge propellant utilization efficiencies), then charge-exchange ions originating downstream of the neutralization plane likely dominate the total impingement current. However, if 40 cm thruster accelerator currents are approximately half those for the NSTAR thruster at similar operating conditions, then charge-exchange ions originating upstream of the neutralization plane dominate the total impingement current.

Table 1. Preliminary 40 cm thruster ion optics' currents and voltages for operation at high R-ratios.[a]

Input Power,[b] kW	Beam Current,[b] A	Beam Voltage,[b] V	Accelerator Voltage,[b] V	Total Voltage,[b] V	Total Voltage Limit,[c] V	Electron Backstreaming Limit,[d] V
10.0	5.80	1567	-257	1824	1196	-217
8.2	4.75	1567	-257	1824	1111	-203
6.1	3.52	1567	-257	1824	994	-186
4.7	2.70	1567	-257	1824	901	-175
2.2	1.20	1567	-257	1824	667	-156
7.4	4.75	1396	-243	1639	1111	-187
5.5	3.52	1396	-243	1639	994	-171
4.2	2.70	1396	-243	1639	901	-160
2.0	1.20	1396	-243	1639	667	-140
4.7	3.52	1179	-227	1406	994	-152
3.6	2.70	1179	-227	1406	901	-141
1.7	1.20	1179	-227	1406	667	-121
3.2	2.70	1021	-216	1237	901	-127
1.5	1.20	1021	-216	1237	667	-107
1.1	1.20	679	-197	876	667	-76

[a]A discharge voltage of 24 V and a flatness parameter of 0.6 were assumed.
[b]Preliminary operating point.
[c]Predicted impingement-limited total voltage based on the average beamlet current.
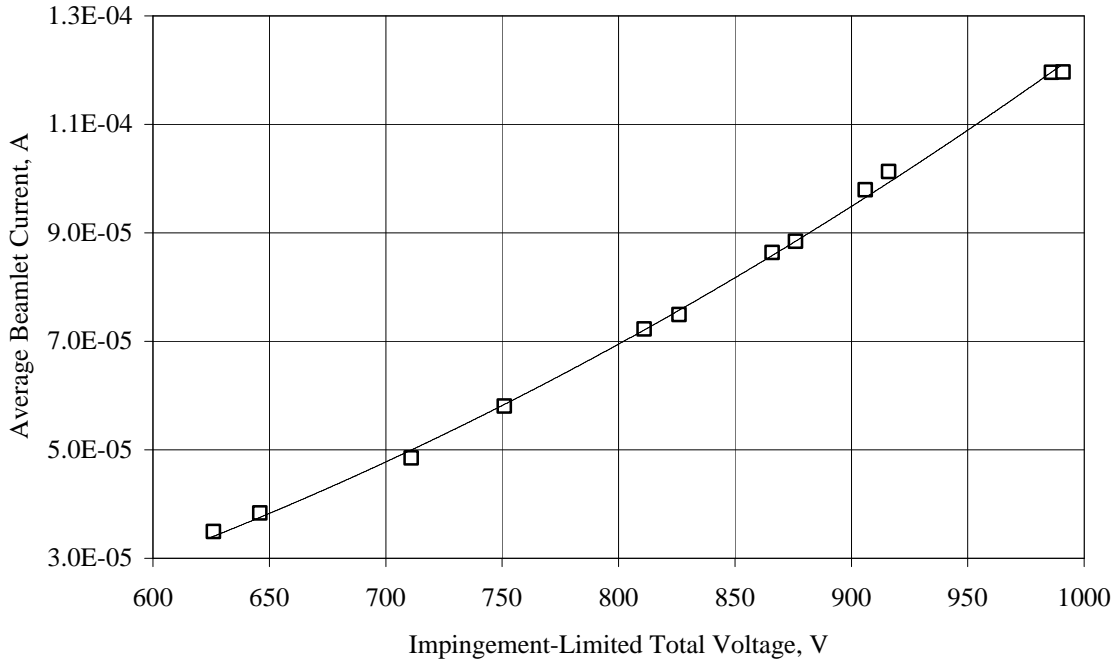[d]Predicted limit.

Fig. 1. Average beamlet current as a function of impingement-limited total voltage for the NSTAR ion optics. Data taken from Refs. [11] and [12].
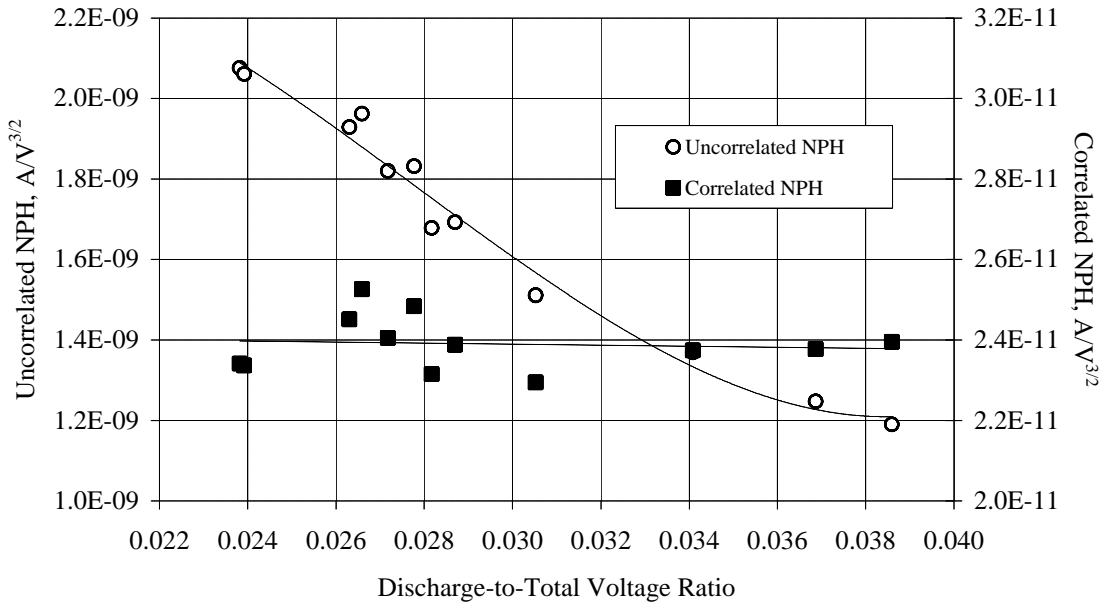

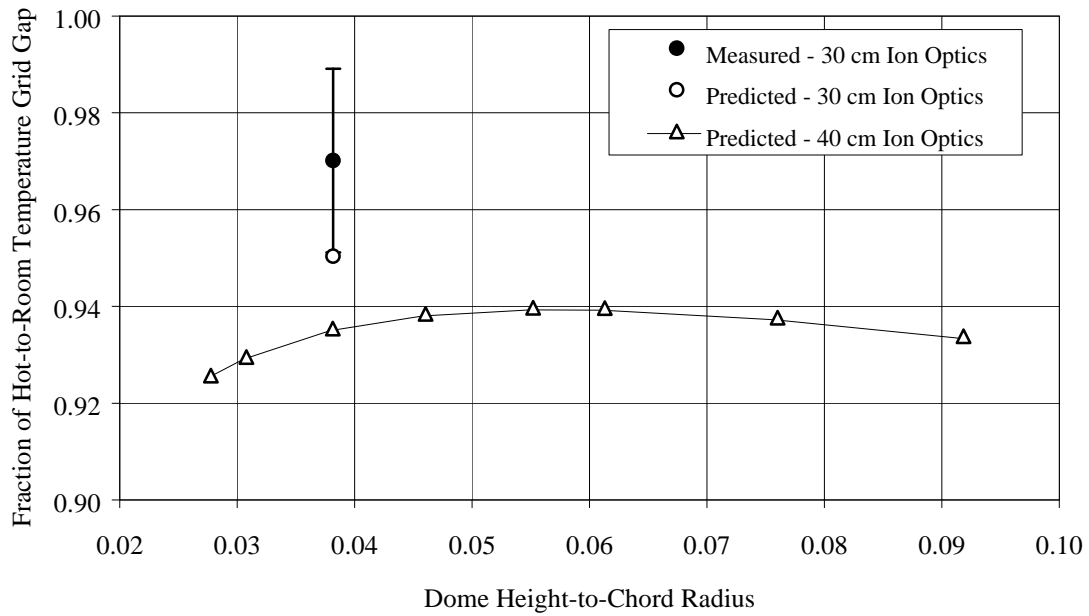**Fig. 2. Normalized perveance per hole as a function of discharge-to-total voltage ratio for the NSTAR ion optics.**

Fig. 3. Fraction of hot-to-room temperature grid gap for 30 cm and 40 cm ion optics. Measured datum is from Ref. [20].
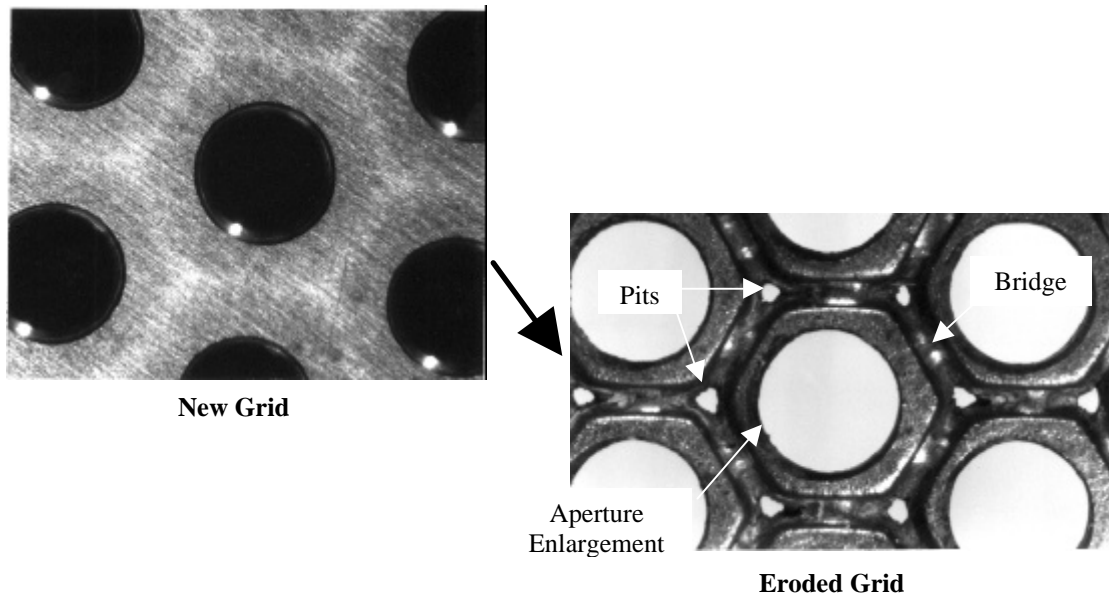

New Grid

Eroded Grid

Fig. 4. Typical accelerator grid erosion sites.

Fig. 5. Ratio of accelerator grid volumetric erosion rate per hole to that of the NSTAR thruster. Discharge chamber propellant utilization efficiencies and flatness parameters are assumed to be the same for all beam extraction diameters.
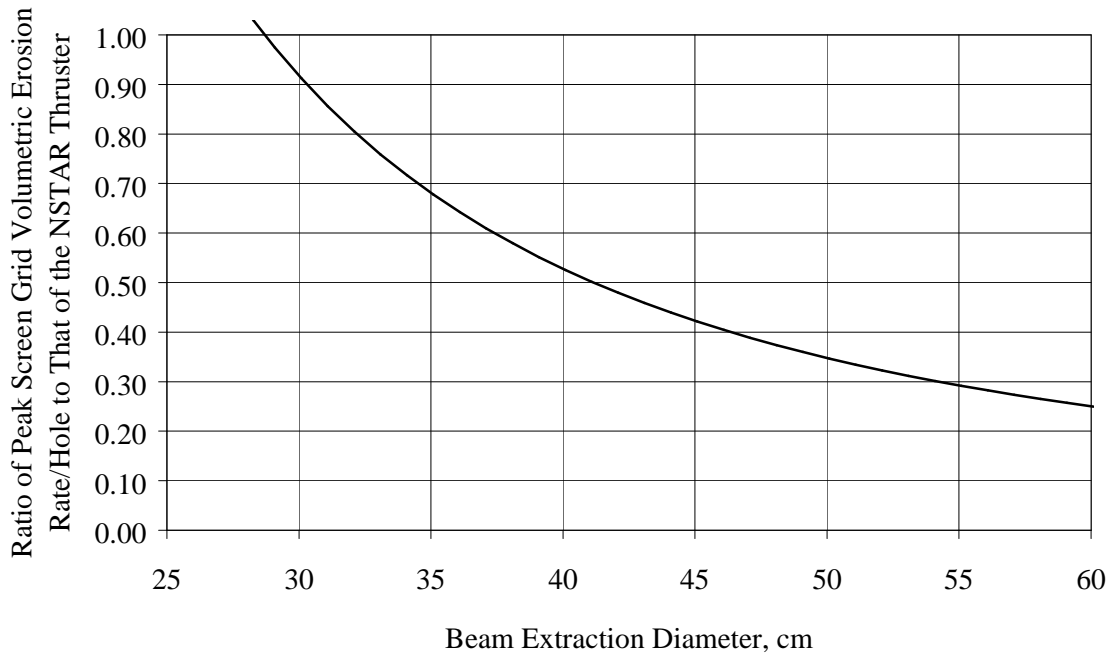

Fig. 6. Ratio of peak screen grid volumetric erosion rate per hole to that of the NSTAR thruster. Screen grid discharge ion transparencies, ratios of doubly-to-singly charged ion currents, discharge voltages, and flatness parameters are assumed to be the same for all beam extraction diameters.

Fig. 7. Photograph of 40 cm screen grid (left foreground) and 40 cm accelerator grid (right foreground) with a 30 cm accelerator grid (center background) for comparison.
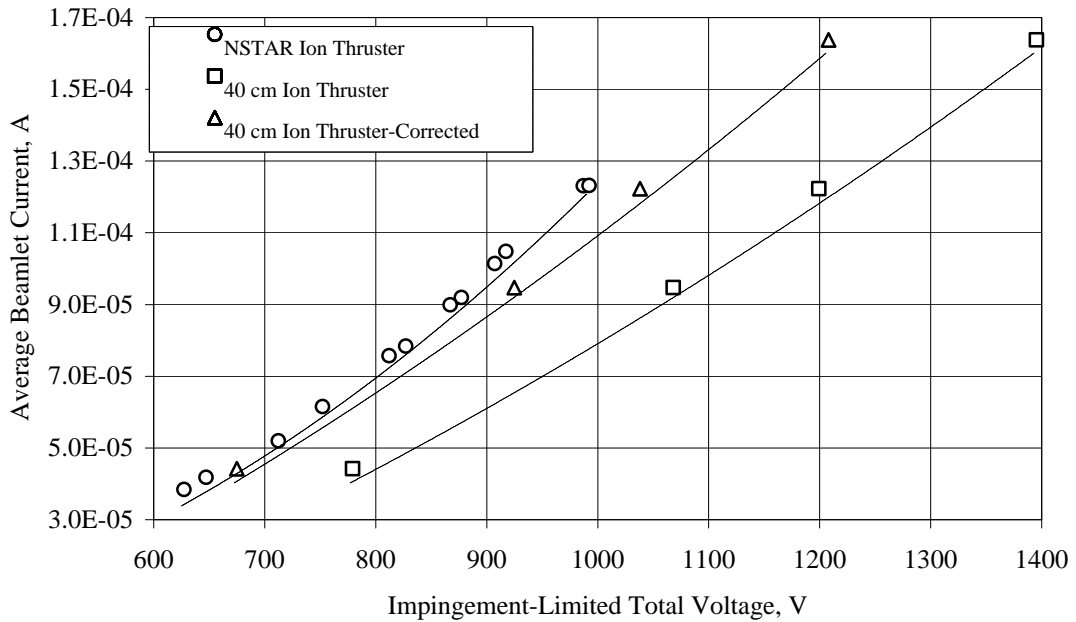

Fig. 8. Average beamlet current as a function of impingement-limited total voltage for the 40 cm and NSTAR ion thrusters. Data for the 40 cm thruster include measured data and data corrected for an NSTAR effective acceleration length.
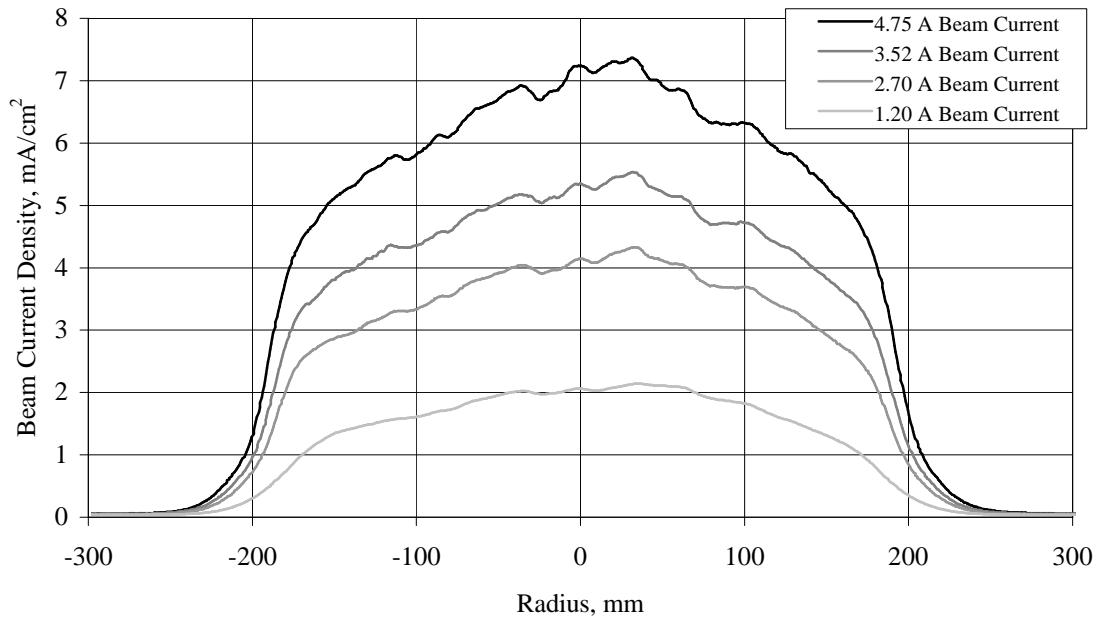
Fig. 9. Radial beam current density profiles for the 40 cm ion thruster at 49 mm downstream of the ion optics' center for beam currents of 1.20 A, 2.70 A, 3.52 A, and 4.75 A.